Lawton, MC., & McGeehan, JP. (1994). The application of a deterministic ray launching algorithm for the prediction of radio channel characteristics in small-cell environments. *IEEE Transactions on Vehicular Technology*, *43*(4), 955 - 968. https://doi.org/10.1109/25.330158

The Application of a Deterministic Ray Launching Algorithm for the Prediction of Radio Channel Characteristics in Small-Cell Environments

Michael C. Lawton and J. P. McGeehan

Abstract—**Propagation characteristics play a fundamental role in the design and implementation of radio systems. The application of broadband digital data services within the cordless environment requires close consideration of the dispersive nature of radio channels. A prediction algorithm is presented such that propagation characteristics can be estimated for small-cell high-data-rate systems. Through the use of geometric optics and geometric theory of diffraction the algorithm performs ray launching techniques in order to evaluate reflected, transmitted, and diffracted rays from a simplified description of a given environment. Both modeled and measured results are presented demonstrating the model's ability to predict typical rms delay spread values.**

I. Introduction

THE LAST decade has seen an unprecedented growth in the use of mobile radio services both in the UK and overseas. This development has been aided by much research interest in the field of mobile telephony. Indeed the success of mobile radio, and in particular, cellular technology calls for yet more research in order that capacity problems arising from the conflicts between the availability of spectrum and the number of users can be solved. In addition to such market demands, the success of radio telephony has prompted considerable research into the application of radio to digital data systems, for example, wireless PBX's, wireless LAN's, digital telephones, and the transmission of digital data throughout factories.

The successful implementation of digital radio systems offering of the order of tens of megabits per second [1] is an exciting prospect. The application of such technologies clearly has huge implications regarding work practices and indeed society as a whole. For example, services such as telecommuting and videoconferencing may become more accessible to individuals, prompting a reduction in their need for travel.

The radio environment is unfortunately a complex and somewhat hostile one for the application of broadband systems. The received signal typically arrives via many separate paths arising from reflections, diffraction, and scattering within the medium. For a narrowband system (where the bandwidth is sufficiently small that the delays between paths can be ignored), the received signal strength is created as a result of the superposition of arriving magnitudes and phases for all the individual paths. For small spatial movements, the phases of individual rays or paths experience different changes governed by the direction of the incoming ray, direction of travel of the mobile receiver, and its distance moved. The rapidly changing phases for each of the individual paths combine to give a fluctuating received signal envelope, a phenomenon termed Rayleigh or fast fading.

Consideration of wideband systems further complicates the channel through the need to assess the frequency selective nature of fading. For separate single tones within a system bandwidth, the arriving phases for individual paths or rays will not be the same. Thus, the magnitude response formed from the superposition of these paths will vary with frequency. This selectivity has the effect of introducing linear distortion into the channel. In the time domain, this distortion can be represented by a complex linear filter, the tap delays of which relate to the path delays and the tap coefficients have a magnitude and phase in agreement with that of the incoming paths. For broadband systems, the delays of the incoming paths can become appreciable with respect to the symbol rate, and intersymbol interference (ISI) can take place. This behavior imposes a maximum limit on the throughput designers can achieve without resorting to techniques to combat the distortion.

The problems of fast fading and ISI have resulted in the need for a more detailed understanding of the radio propagation environment. This has brought about widespread research interest in the propagation measurement and modeling of both cellular and cordless radio systems.

The field of propagation measurement is quite well documented, with several authors [2]–[4] having measured both narrow and wideband channel soundings for a range of different environments. This work is on-going with much data still needed in order to characterize new frequencies and cell topographies. The continuing demands placed on the radio spectrum, in terms of frequency allocation and service provision, require system designers to consider the use of new frequency bands, for example, millimeter waves, and consequently new measurements are required [5]. In addition, the trend towards more spectrally efficient small cells calls for yet more measurement data.

The area of mobile radio propagation modeling has also been actively researched throughout the last three decades

Manuscript received July 16, 1992; revised September 18, 1992 and June 17, 1993.

M. C. Lawton was with the Centre for Communications Research at Bristol University. He is now with Hewlett-Packard, Hewlett-Packard Laboratories, Bristol BS12 6QZ, United Kingdom.

J. P. McGeehan is with the Centre for Communications Research, Faculty of Engineering, University of Bristol, Bristol BS8 1TR, United Kingdom.

IEEE Log Number 9403316.

providing many useful models. This work can be broadly divided into two categories, those of simulation and prediction models.

With simulation, researchers initially take measurements and characterize a typical environment. An attempt is then made to find a mathematical model which agrees with the measured data. This can then be optimized for different environments and comparisons made. This was the approach initially adopted by Turin [6] and improved by both Suzuki [7] and later Hashemi [8]. A similar method has been used by Ganesh and Pahlavan [9] for the indoor environment. This approach has attracted considerable research effort in recent years, and a variety of useful simulation tools is now readily available in the literature [10]. The simulation approach is very useful but it does have limitations. The model cannot easily be changed for different environments and often involves further measurements.

Predictions models attempt to overcome this limitation by some form of environmental description as an input to the model. An attempt is then made to provide a model which analytically evaluates propagation characteristics similar to what might be expected for any given cell. Work has been done by Zander [11], and later by Bajwa [12], where the average street width is used as an input to the model. A predictive algorithm was also developed by Gladstone and McGeehan [13], [14], where ray tracing was used to estimate narrowband patterns, in both single and multi-transmitter mobile radio systems. While a ray tracing approach is simple to implement, it is computationally time consuming and often not practical. However, recent technological advances in computing, combined with an interest in new high data rate small cells make ray tracing an attractive option [15], [16].

In this paper, a ray tracing algorithm for the prediction of propagation characteristics in cordless applications is presented. This is suitable for cordless environments, both indoors and outdoors up to a cell radius of around 150 m.

II. The Propagation Model

The equation used to describe the channel was first proposed by Turin [6] and has subsequently been used by several authors [7]–[9]. It takes the form of a bandlimited complex impulse response $h(t)$ given by

$$h(t) = \sum_{k=1}^{n} \alpha_k . \delta(t - \tau_k) . \exp(j\Phi_k). \tag{1}$$

Here, the transmitted pulse is mathematically described by a Dirac function and the received signal $h(t)$ is formed from the addition of a number of time-delayed paths, each represented by an attenuated and phase-shifted Dirac waveform. The method adopted in this paper directly seeks to evaluate suitable path parameters for the amplitude α_k, arrival time τ_k, and the arrival phase Φ_k, such that the propagation characteristics can be predicted. This algorithm evaluates reflected and transmitted paths through the use of geometric optics, and, in addition, diffracted rays are calculated using the geometric theory of diffraction.

A. Geometric Optics

Geometric optics is an approximate high-frequency technique for determining the magnitude of incident, reflected, and refracted fields. The technique uses ray tracing techniques in order to calculate the energy from significant paths between the transmitter and the receiver. The signal amplitude for each of the radiating rays is assumed to attenuate reciprocally with the path distance and additional losses are calculated upon reflection, transmission, or diffraction within the environment. In order to increase the algorithm speed, it was decided to place a limitation such that only reflecting surfaces parallel to the x, y, or z axes were treated. This limitation was deemed acceptable because most building structures tend to be formed from walls which are perpendicular to one another. To make the algorithm as realistic as possible the reflection and transmission characteristics have been evaluated as a function of incident angle for a range of different wall materials. The algorithm has also been made more useful to system designers by giving both the receiving and transmitting antennas gain patterns. Both antennas were modeled as vertically polarized half-wave dipoles.

The resulting magnitude and phase of these rays can then be inserted, as α_k and Φ_k values, respectively, in (1).

1) Reflection and Transmission Characteristics: With any ray tracing technique it is necessary to calculate the loss arising from reflections and/or transmissions within a medium. For the work described here, an attempt was made to calculate deterministically the reflection and transmission coefficients, as a function of incident angle, for the various obstacles within the environment. In order to do this, it was necessary to characterize electrically the various materials existing within the environment. For this, the model uses four parameters to describe each wall, namely, the relative electric permittivity (ϵ_r), the relative magnetic permeability (μ_r), the conductivity (σ), and the wall thickness (d). The user is offered the choice of inputting dielectric properties to suit particular needs or selecting walls from a list of prespecified *standard* wall types offered within the model. The five standard wall types and their characteristics are given in Table I.

Table I was generated after considering the data from several sources [17], [18] and analyzing their resulting reflection and transmission coefficients. For thick and thin walls, wide variations in reported permittivity and conductivity values were found. The conductivity varied from 0.001 [19] to 7 [20], and the relative permittivity from 4 [19] to 15 [20]. These parameters must be heavily dependent upon the exact constituents of a given material and the frequency of use, and hence, their accuracies are doubtful. In addition, the parameters change with weather conditions, for example, increased loss and reflectivity following rain or snow. For the research described here, measured values for particular walls were not available and judgments were made on suitable values. These were taken from the literature quoted in the above table. The reflection and transmission coefficients have also been calculated for each of these wall materials and these are shown in Figs. 1–4. The figures for the permittivity and conductivity for the thick and thin walls were taken from an approximation of the characteristics of the earth.

TABLE I
THE DIELECTRIC PROPERTIES USED FOR SPECIFIED WALL TYPES WITHIN THE MODEL

Wall Type	Rel. permittivity	Rel. permeability	Conductivity	Thickness	Reference
	$\epsilon_r,(Fm^{-1})$	$\mu_r,(Hm^{-1})$	$\sigma,(Am^{-2})$	$d,(m)$	
Thick wall	9	1	0.1	0.35	Ballanis p208
Thin wall	9	1	0.1	0.15	Ballanis p208
Wooden panel	5	1	0	0.03	Smulders [17]
Glass	2.4	1	0	0.003	Ballanis p50
Copper Sheet	1	1	5.76e7	0.003	Ballanis p212

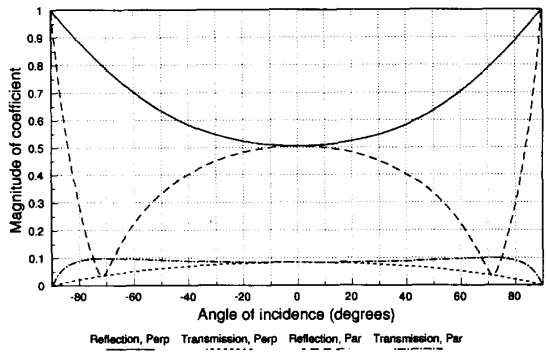

Fig. 1. Reflection and transmission coefficients for a thick wall within the model.

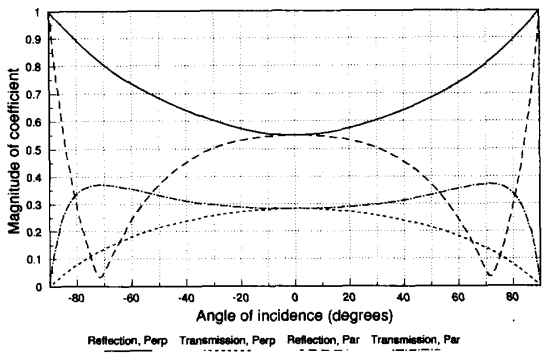

Fig. 2. Reflection and transmission coefficients for a thin wall within the model.

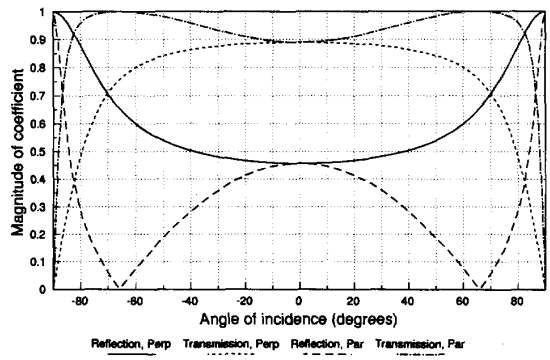

Fig. 3. Reflection and transmission coefficients for a wooden partition within the model.

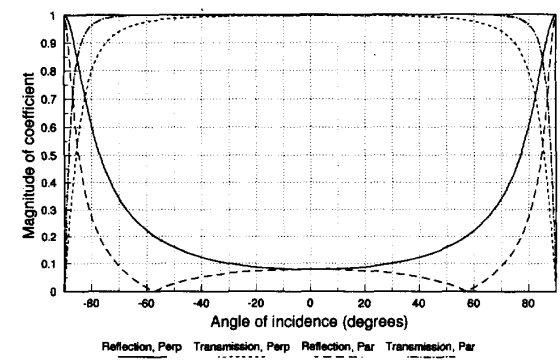

Fig. 4. Reflection and transmission coefficients for a glass window within the model.

The calculation to evaluate the reflection and transmission characteristics of the material is performed using a ray tracing technique described in Fig. 5. This figure shows a dielectric slab, (medium 2) representing the wall, with air on either side of it (mediums 1 and 3). An incident ray arrives at the wall with an angle θ_i. This ray then divides into two rays, a reflected ray Rf_1 which departs at angle θ_r (equal to θ_i) from the normal and a transmitted ray within the wall itself. This ray is bent towards the normal and has a refraction angle ψ. This ray then travels through the wall, which if it is lossy will attenuate the ray, before reaching the wall–air interface. Here, the ray divides again generating a transmitted ray Tr_1 and an internally reflected ray. The internally reflected ray continues within the medium undergoing multiple reflections, and for a lossy medium, being progressively attenuated. The ray tracing technique used for the reflection calculations evaluates the contributions of the various transmitted $(Tr_1, Tr_2, Tr_3 \cdots)$ and reflected rays $(Rf_1, Rf_2, Rf_3, \cdots)$ until they become insignificantly small (i.e., 1 ppm). The reflected rays and the transmitted rays are then combined, by vector addition, to give a single transmitted ray and reflected ray. The algorithm simplifies the problem by joining all the transmitted and reflected rays to form paths shown with large solid arrows in Fig. 5. These represent both the reflected and transmitted energies.

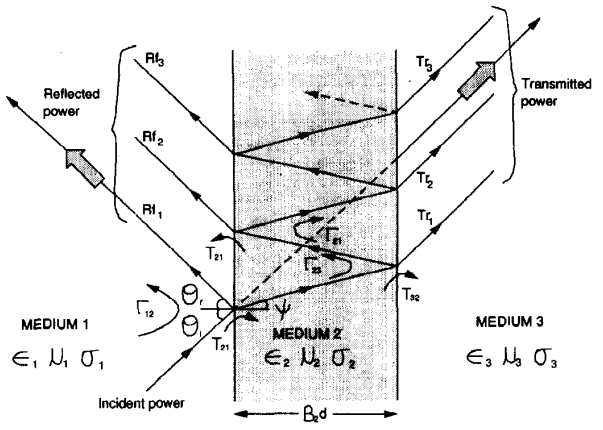

Fig. 5. Transmitted and reflected rays for an oblique incident wave on a conducting dielectric slab.

In order to calculate the magnitude and phase of each of these rays, it is necessary first to evaluate the reflection and transmission coefficients across each of the boundaries. A general expression for the reflection coefficient, for perpendicular polarization, at the boundary 1–2, can be expressed as [18]

$$\Gamma_\perp = \frac{E_\perp^r}{E_\perp^i} = \frac{\eta_2 \cos\theta_i - \eta_1 \cos\theta_t}{\eta_2 \cos\theta_i + \eta_1 \cos\theta_t} \tag{2}$$

where η = the wave impedance = $\sqrt{\mu/\epsilon}$ and θ_t equals the angle of transmission, which may be a complex number. The transmission coefficient across the same boundary is given by [18]

$$T_\perp = \frac{E_\perp^t}{E_\perp^i} = \frac{2\eta_2 \cos\theta_i}{\eta_2 \cos\theta_i + \eta_1 \cos\theta_t}. \tag{3}$$

In addition, the corresponding equations for parallel polarization are, for the reflection coefficient [18],

$$\Gamma_\parallel = \frac{E_\parallel^r}{E_\parallel^i} = \frac{-\eta_1 \cos\theta_i + \eta_2 \cos\theta_t}{\eta_1 \cos\theta_i + \eta_2 \cos\theta_t} \tag{4}$$

and for the transmission coefficient [18]

$$T_\parallel = \frac{E_\parallel^t}{E_\parallel^i} = \frac{2\eta_2 \cos\theta_i}{\eta_1 \cos\theta_i + \eta_2 \cos\theta_t}. \tag{5}$$

These equations are relatively straightforward for lossless materials. For lossy materials, however, ϵ and θ_t become complex (i.e., of the form $a + jb$). The electric permittivity ϵ is then given by the equation [18]

$$\epsilon = \epsilon_r - j\frac{\sigma}{2\pi f} \tag{6}$$

where f = the frequency, and θ_t is the refraction angle can be calculated using Snell's law of refraction, that is,

$$\gamma_1 \sin\theta_i = \gamma_2 \sin\theta_t \tag{7}$$

where γ is the propagation constant and is made up of both real and imaginary parts. The real part (α_2) is referred to as the attenuation constant and the complex part (β_2) is known as the phase constant. For a lossless material $\alpha_2 = 0$ and hence both $\sin\theta_i$ and $\sin\theta_t$ are real. However, if $\alpha <> 0$, then the complex terms do not cancel and the propagation constant and $\sin\theta_t$ are both complex. The observed angle of a transmitted ray within the conducting material is shown in Fig. 5 as ψ with the angle θ_t being a complex figure. The mathematical derivation for the observed angle is given by Ballanis [18], who concludes that the angle of the transmitted ray ψ (see Fig. 5) is determined by the following relations:

$$\sin\psi = \frac{\beta_1 \sin\theta_i}{\sqrt{(\beta_1 \sin\theta_i)^2 + q^2}} \tag{8}$$

and

$$\cos\psi = \frac{q}{\sqrt{(\beta_1 \sin\theta_i)^2 + q^2}} \tag{9}$$

where q is determined by

$$q = s(\alpha_2 \sin\zeta + \beta_2 \cos\zeta) \tag{10}$$

with s and ζ related by the following equation:

$$\cos\theta_t = \sqrt{1 - \sin^2\theta_t} = \sqrt{1 - \left(\frac{j\beta_1}{\alpha_2 + j\beta_2}\right)^2 \sin^2\theta_i}$$
$$= s\exp(j\zeta) = s(\cos\zeta + j\sin\zeta). \tag{11}$$

The above reflection and transmission calculations are performed within the algorithm and values are stored in a 90-element array. These coefficient values are then applied as additional losses in order to calculate the arriving signal strength for a given ray.

2) The Image Technique: In order to perform the ray tracing, a technique similar to that of the method of images has been developed. Rather than use an approximate technique where many rays of similar angles are plotted away from the transmitter, the technique adopted here considers walls and obstacles as potential reflectors and hence evaluates transmitter images. There are several advantages offered by this technique. First, the method is analytical and not approximate and as such is more reliable and more accurate. With an approximate technique it is necessary for the receiver to have a finite size. If its area is too small, then the algorithm may not find all the available paths. Conversely, if the receiver is too large, then paths may be duplicated. With the analytical technique, the receiver is placed at an infinitesimally small point such that paths are neither duplicalted nor missed, and each path is calculated precisely. The analytical technique can also easily be extended to include the contribution from transmitted rays (method described later). Finally, for simple environments, the various permutations of reflecting walls are significantly fewer than the number of paths which need to be considered to give a similar result using approximate techniques.

Conceptually, the algorithm works by reflecting the transmitter about permutations of reflecting walls and evaluating the corresponding transmitter images. Information about the images is then stored in an array and used for all receiver locations. For each receiver, location lines are then drawn between the receiver and transmitter images (Fig. 6). If these lines are intersected by the reflecting wall or walls and no

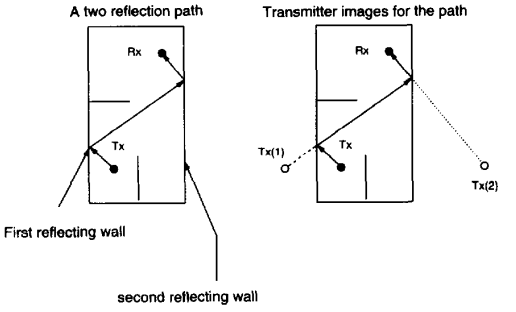

Fig. 6. Representation of a two reflection path within the algorithm.

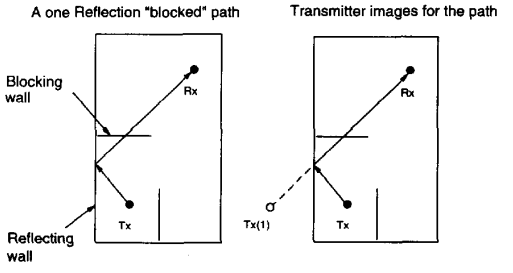

Fig. 7. Representation of a one reflection transmitted path within the algorithm.

other walls, then a *purely reflected* path is said to exist. The value of τ_k for the path is found from the length of the lines and the speed of light. The value of α_k is found by using a square law attenuation for signal power with distance and incorporating a reflection loss. Φ_k can be evaluated from the path length and the carrier frequency with adjustments for phase transitions following reflection or diffraction. In the event of the lines between reflected transmitter images and receiver being intersected by all reflecting planes and additional planes, then a path is still said to exist but is further attenuated by passing through a blocking wall or walls (Fig. 7).

Previous work has been reported by the authors [21] where the model was used for the prediction of radio channel characteristics for indoor cells. In such cells, it was necessary to have a 3-D model such that multiple ceiling-floor reflections could be modeled. For the outdoor application described in this paper, it was decided to adapt the model for a 2-D environmental description. In doing this, an assumption is made that the transmitter is below roof top height and therefore roof top dimensions need not be inputted as no path can pass over a building. However, while all the reflectors are described in terms of only two dimensions, the ground is still represented within the model. For each path found, an additional path corresponding to the same path with an extra ground reflection is added. Hence, receiver and transmitter heights are still needed as inputs to the model. The algorithm is divided into two main areas. For an initial receiver location, the algorithm evaluates transmitter images, up to a maximum of seven orders of reflection and stores the data. Having calculated all the transmitter image locations, the algorithm moves into its second phase where it simply uses the image data at any given receiver location and tests for valid paths.

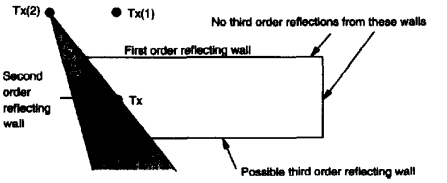

Fig. 8. Illustration of technique used to validate possible image permutations.

The stored images are calculated in a hierarchical fashion by generating an image tree. The image tree is a *tree-like* diagram which gives each of the images capable of providing a path for each order of reflection. In order to generate this table, each calculated image is tested in order to establish whether it is capable of providing a path. If this test proves false, then the image is not stored and the algorithm ignores all higher order permutations which begin with the same wall sequence. The method for testing an image is shown in Fig. 8. The diagram shows the first and second reflecting walls and their corresponding images. Two lines have been drawn from the second-order image to the two edges of the second-order wall. These two lines form an arc (shaded in the figure) which describes the area which is illuminated by the second-order image. Only walls which intersect this area are considered as subsequent third-order images. This technique is useful for reducing the size of the image table and hence the run time of the algorithm.

B. Geometric Theory of Diffraction

The application of geometric optics provides a simple and effective method for predicting the behavior of radio channels. The method is, however, approximate and has limitations. For a non-LOS scenario, geometric optics suffers from its exclusion of the diffracted ray paths. It was felt that in the frequency band considered here (center frequency 1.845 GHz), the effect of the diffracted rays may well be significant and thus warranted investigation. Over the last 60 years, many techniques for evaluating edge diffraction terms have been presented in the literature. Perhaps the most widely known of these is the method of Fresnel knife edge diffraction. This technique was first proposed by Schelling *et al.* [22] and is still used widely today. The technique does, however, ignore some important parameters such as polarization, edge conductivity, edge permittivity, and ridge profile, all of which are available as information within the framework of the basic geometric optics model. Another approach to diffraction modeling which does not suffer such limitations is the geometric theory of diffraction (GTD). This was first proposed by Keller [23] some 20 years ago and has since been improved by Kouyoumjian and Pathak [24] such that inaccuracies close to the incident and reflection boundaries are removed. In addition to this, further work has been done by Leubbers [25] so that the GTD formulation can readily be applied to wedges of finite conductivity.

GTD owes its origins to Keller's attempts to improve on geometric optics and has been designed as an extension to a geometric optics approach. Thus, the two methods can be

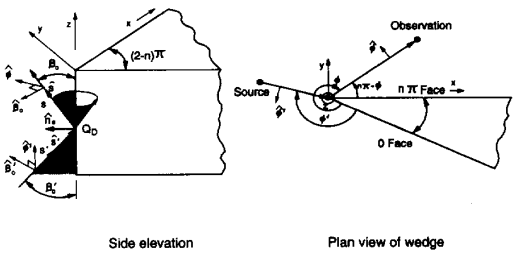

Fig. 9. Geometry and coordinates for application of GTD.

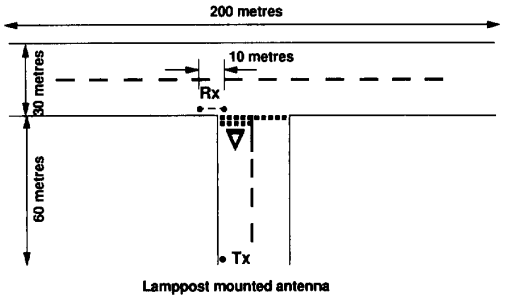

Fig. 10. Representation of "T" junction within the algorithm.

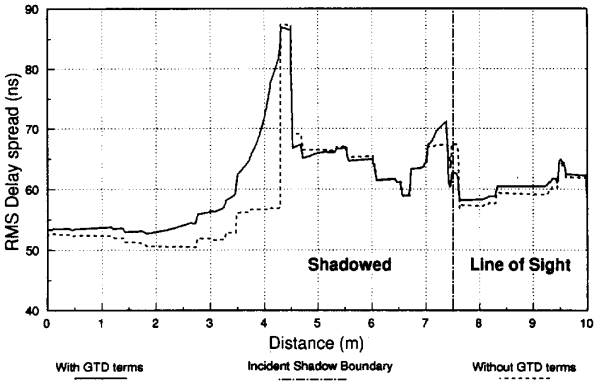

Fig. 11. Variation in rms delay spread with distance for the environment in Fig. 10. Note incident shadow boundary at 7.5 m.

elegantly combined to provide a single prediction tool. The formulation of diffracted paths is similar to that of reflected paths in geometric optics except that the reflection coefficient $\overline{R}$ is replaced with a dyadic diffraction coefficient $\overline{D}$, i.e., a two-by-two matrix. Also, alterations are made to the spatial attenuation factor.

The diffracted field at the observation point is given by [18]

$$E^d(s) = \underbrace{E^i(Q_D)}_{\substack{\text{Field at}\\ \text{reference}\\ \text{point}}} \cdot \underbrace{\overline{D}}_{\substack{\text{Diffraction}\\ \text{coefficient}\\ \text{(usually a}\\ \text{dyadic)}}} \cdot \underbrace{A(\rho_c, s)}_{\substack{\text{Spatial}\\ \text{attenuation}\\ \text{(spreading,}\\ \text{divergence)}\\ \text{factor}}} \cdot \underbrace{e^{-j\beta s}}_{\substack{\text{Phase}\\ \text{factor}}} \quad (12)$$

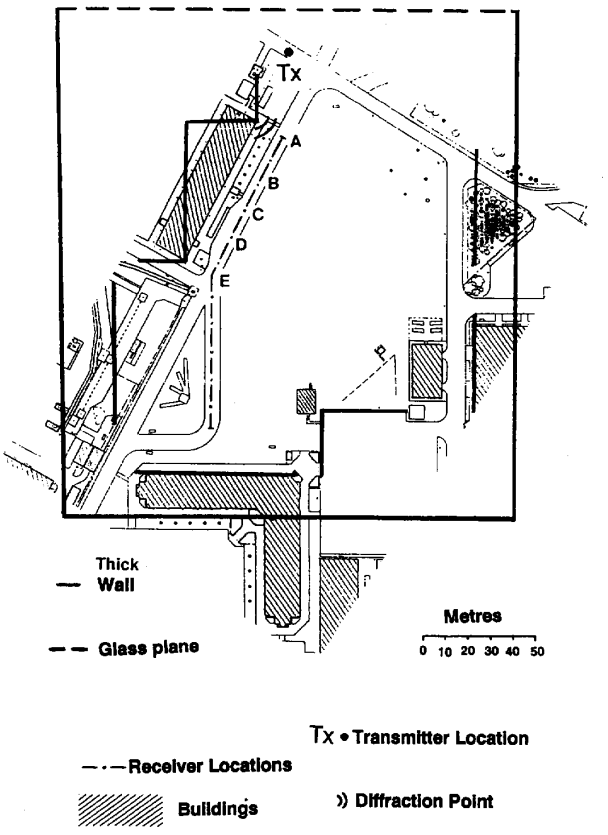

Fig. 12. Environmental description for site 1 (heavy lines show representation of obstacles within the model).

where

$$A(\rho_c, s) = \sqrt{\frac{\rho_c}{s(\rho_c + s)}} \quad (13)$$

and ρ_c represents the distance between the reference point $Q_D(s = 0)$ at the edge (also first caustic of the diffracted rays) and the second caustic of the diffracted rays. For the straight edge diffraction application used within the model, the equation simplifies to [18]

$$E^d(s) = E^i(Q_D)\overline{D}A(s', s)e^{-j\beta s} \quad (14)$$

where

$$A(s', s) = \sqrt{\frac{s'}{s(s + s')}} \quad (15)$$

for spherical wave incidence and s, s', and β_0, β_0' are as shown in Fig. 9. β_0' is the oblique angle of incidence of the arriving ray with respect to the diffracting edge and β_0 is the angle formed by the departing rays and the diffracting edge. Note that for spherical wave incidence $s' = \rho_c$.

For a perfectly conducting wedge, the diffraction coefficient $\overline{D}$ for observation points not too close to the incident or

reflection boundaries is given by [23]

$$D_s = \frac{\exp^{(-j\pi/4)}\frac{1}{n}\sin\left(\frac{\pi}{n}\right)}{\sqrt{2\pi\beta}}\left[\frac{1}{\cos\left(\frac{\pi}{n}\right)-\cos\left(\frac{\phi-\phi'}{n}\right)} - \frac{1}{\cos\left(\frac{\pi}{n}\right)-\cos\left(\frac{\phi+\phi'}{n}\right)}\right] \tag{16}$$

for soft polarization (E-field parallel to both faces of the wedge) and for hard polarization (H-field parallel to the wedge faces), D_h

$$D_h = \frac{\exp^{(-j\pi/4)}\frac{1}{n}\sin\left(\frac{\pi}{n}\right)}{\sqrt{2\pi\beta}}\left[\frac{1}{\cos\left(\frac{\pi}{n}\right)-\cos\left(\frac{\phi-\phi'}{n}\right)} + \frac{1}{\cos\left(\frac{\pi}{n}\right)-\cos\left(\frac{\phi+\phi'}{n}\right)}\right] \tag{17}$$

where ϕ' and ϕ are the angles of incidence and $n\pi$ is the exterior wedge angle (see Fig. 9). The diffracted field, for either soft or hard polarization, resulting from a finitely conducting wedge can be calculated without the singularity problems at the incidence and reflection boundaries [25] using

$$\begin{aligned} D_s^h = {} & \frac{-\exp^{(-j\pi/4)}}{2n\sqrt{2\pi\beta}\sin\beta_0'} \\ & \cdot\left\{\cot\left[\frac{\pi+(\phi-\phi')}{2n}\right]F(\beta Lg^+(\phi-\phi')) \right. \\ & + \cot\left[\frac{\pi-(\phi-\phi')}{2n}\right]F(\beta Lg^-(\phi-\phi')) \\ & + R_{0\perp}^{\parallel}\cdot\cot\left[\frac{\pi-(\phi+\phi')}{2n}\right]F(\beta Lg^-(\phi+\phi')) \\ & \left. + R_{n\perp}^{\parallel}\cdot\cot\left[\frac{\pi+(\phi+\phi')}{2n}\right]F(\beta Lg^+(\phi+\phi'))\right\} \end{aligned} \tag{18}$$

where the Fresnel transition function

$$F(x) = 2j\sqrt{x}\exp^{jx}\int_{\sqrt{x}}^{\infty}\exp^{-j\tau^2}\,d\tau \tag{19}$$

and

$$L = \frac{ss'\sin^2\beta_0'}{s+s'}, \quad g^{\pm}(k) = 2\cos^2\left(\frac{2n\pi N^{\pm}-k}{2}\right), \quad k = \phi\pm\phi'. \tag{20}$$

In (20), $N^{\pm}$ are the integers which most closely satisfy the equations

$$2\pi nN^+ - (k) = \pi \quad \text{and} \quad 2\pi nN^- - (k) = -\pi. \tag{21}$$

In Fig. 9, $R_{0\perp}^{\parallel}$ and $R_{n\perp}^{\parallel}$ are the reflection coefficients for either perpendicular or parallel polarization for the "0" face, incident angle ϕ', and for the n face, reflection angle $(n\pi-\phi)$. Although the mathematical expressions for the diffraction terms look complicated, they can quite readily be evaluated with a computer. Calculation of the diffracted fields does, however, add further complexity to the algorithm and it was felt necessary to limit the computation performed. Consequently, the algorithm described evaluates the first- and second-order diffraction terms along with all combinations of one reflection and one diffraction. For each diffracted path calculated, a similar path with an additional ground reflection is also evaluated.

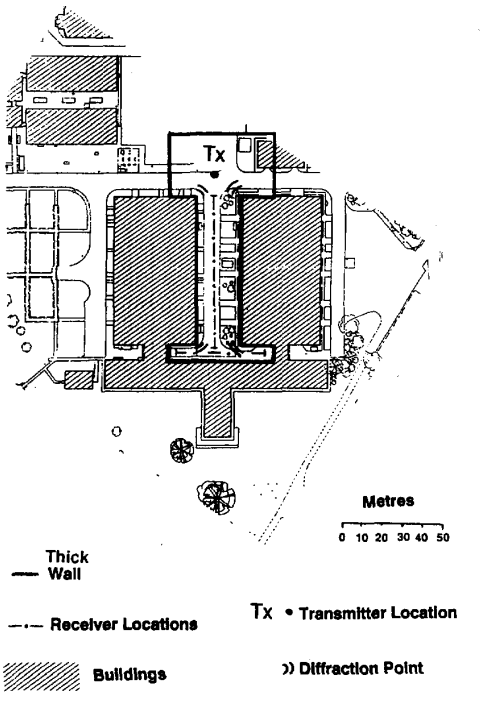

Fig. 13. Environmental description for site 2 (heavy lines show representation of obstacles within the model).

In order to consider the effect of adding diffracted rays to the algorithm, a hypothetical street corner was modeled. Fig. 10 shows a "T" junction with a base station. The receiver was moved along the line indicated and both the signal strength and the RMS delay spread values were calculated. Fig. 11 shows the rms delay spread variations (the rms delay spread is a commonly used measure of time dispersion for a transmitted pulse across a given channel [3]) as the mobile receiver moves around the corner shown in Fig. 10. The solid lines show the result for both reflected and diffracted terms and the dashed lines show the curve with just the reflected terms. Clearly the rms delay spread curves show similarities between the predictions with the diffracted terms and those without; indeed for the LOS region the two methods yield very similar results. Within the shadowed areas the GTD terms add more multipath which results in a more gradual *step-like* wave than that for the rms delay spread plot without the diffracted terms. In the event of using the model as a design tool, then it appears as if diffraction terms are having only a small effect on the range

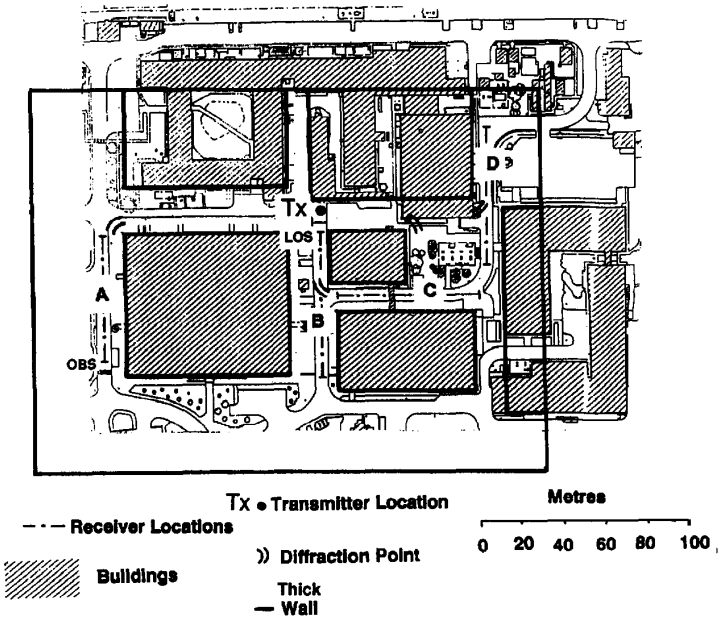

Fig. 14. Environmental description for site 3 (heavy lines show representation of obstacles within the model).

of modeled results and it would probably be worth including the diffracted paths only as an option which can be selected depending upon the circumstances of the modeling scenario.

III. Channel Sounding Measurements

A. Measurement Equipment

A detailed description of channel sounders and sounding techniques will not be presented here. A comprehensive review of sounding techniques can be found in a paper published by Parsons *et al.* [26].

The measurements presented in this paper were taken using a correlation sounder built by British Telecom at their research laboratories in Martlesham, Suffolk (UK). The specification details of the sounder used is as follows:

- 20 Mbs^{-1} clock rate for the PN sequence.
- 31-dB measured dynamic range.
- 100-ns full pulsewidth.
- Maximum output power = 1 W.
- Sleeved dipole antenna used.
- Scaling factor $k = 20{,}000$ (k scales the rate at which the autocorrelation function is produced in time).
- 255-b sequence length.
- 3.8-km maximum range.
- Doppler shift resolution = ± 1.96 Hz.
- Direct conversion receiver.

B. Measurement Sites

Three outdoor measurement sites were both measured and modeled and their details are shown in Figs. 12–14. These sites were chosen because they represent three quite different but typical cordless operating environments for communications.

1) Site 1 (see Fig. 12): This site was chosen because it is an open site with an LOS path and only a few principal reflectors. The site is typical of an open public area, such as a stadium entrance or motorway services. The area behind the transmitter (Tx indicated by a dot in Fig. 12) is flat grassland with no possible reflectors. The environmental description for the purposes of the model is shown in heavy lines on top of the site map. Principal reflectors, diffraction points, and receiver locations are all indicated. Reflecting walls are shown around all buildings within the site and also around a car park which was felt to be potentially offering strong reflected paths. In addition, a reflecting wall was used in place of a small collection of trees. Because all reflectors must lie parallel to either the x, y, or z axes, it has been necessary to approximate to the building closest to the transmitter with a stepped configuration. The outer cell dimensions have been bounded by reflecting planes on three of the four sides. It was felt that for the built-up locations, with these low antenna heights (transmitter height = 2.5 m, receiver height = 1.5 m), it was more likely for dissipating rays to encounter obstacles than to continue in free space. An exception was made for site 1, however, because the area behind the transmitter has no possible reflectors; here, a glass plane was used within the model.

2) Site 2 (see Fig. 13): This site is the smallest of the three sites chosen for investigation and is typical of a site serving a building entrance. The transmitter was placed at the end of a roadway which provided the entrance to a large "U"-shaped building. The area behind the transmitter (i.e., remote from the building entrance) is a car park offering many potential scatterers. Consequently, the description within the model has quite close surrounding walls around it. Measurement of both LOS and obstructed (OBS) profiles were taken as indicated on

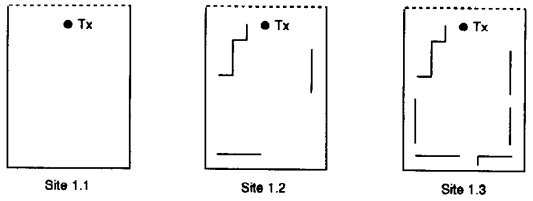

Fig. 15. Different site descriptions used to describe site 1 in order to test the sensitivity of the algorithm.

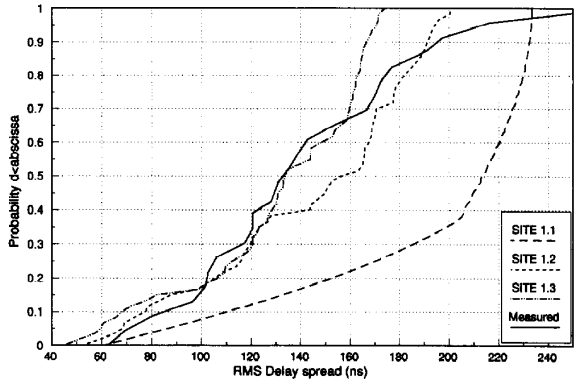

Fig. 16. RMS delay spread variations for the three sites shown in Fig. 15.

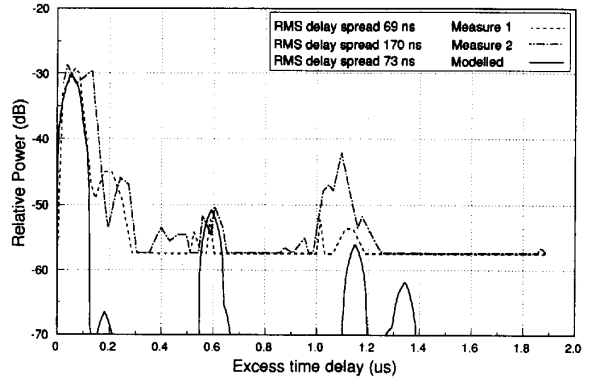

Fig. 17. Measured and modeled power delay profiles at position A which has a transmitter-receiver separation of 35 m (site 1).

the diagram. The environmental description within the model is also shown in the figure (see Fig. 13).

3) Site 3 (see Fig. 14): This cell is smaller than that of site 1 but consists of a much more complicated building pattern. This area was chosen in an attempt to model a more complicated scenario which might be expected in a street location. A combination of both LOS and OBS profiles was measured along the four lines shown (Fig. 14(a)–(d)). The various buildings, which are shown as shaded areas in the diagram, varied in their size and construction. All buildings were, however, higher than both the transmit and receive antennas.

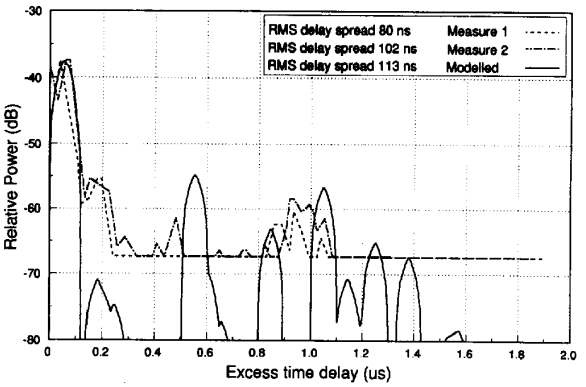

Fig. 18. Measured and modeled power delay profiles at position B which has a transmitter-receiver separation of 60 m (site 1).

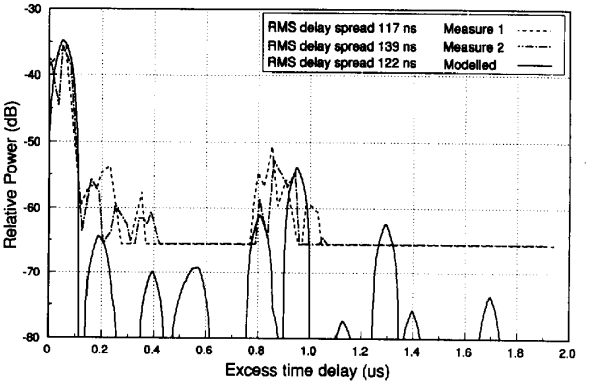

Fig. 19. Measured and modeled power delay profiles at position C which has a transmitter-receiver separation of 60 m (site 1).

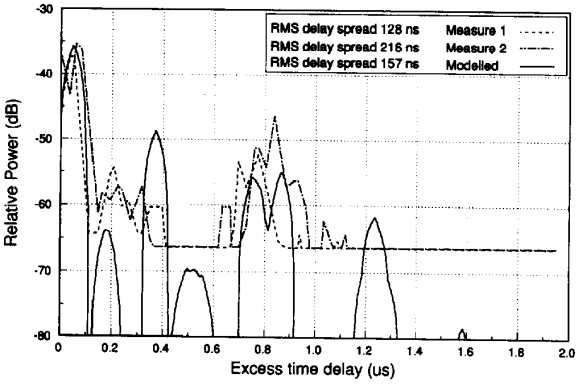

Fig. 20. Measured and modeled power delay profiles at position D which has a transmitter-receiver separation of 75 m (site 1).

IV. The Modeling Process

For each of the three sites shown in Figs. 12–14, the algorithm used a simplified expression for the environment. In order to understand the extent to which the simplification affects the accuracy of the results, site 1 has been considered with several different simplified environmental descriptions (see Fig. 15).

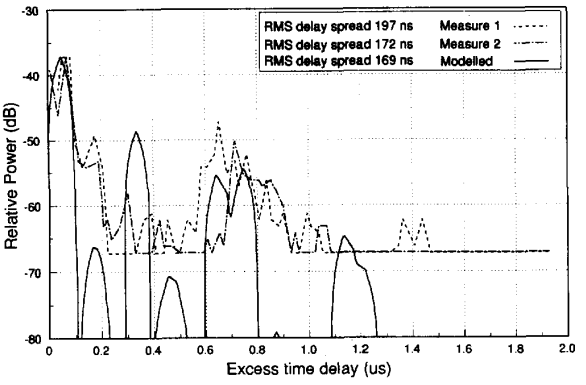

Fig. 21. Measured and modeled power delay profiles at position E which has a transmitter-receiver separation of 90 m (site 1).

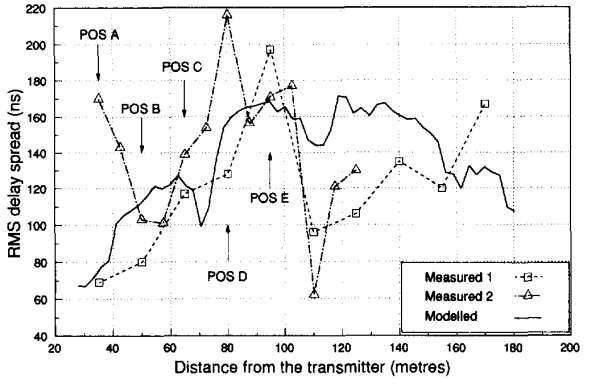

Fig. 22. Measured and modeled power delay profiles versus distance (showing measurement points A–E) for site 1.

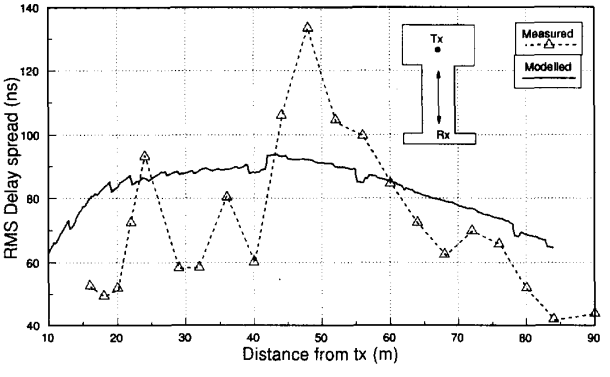

Fig. 23. Modeled and measured variation in rms delay spread with distance for site 2.

Fig. 16 shows the rms delay spread figures, represented as a cumulative distribution function for the different environments. Three sites of differing complexity were considered. Site 1.1 consists of an open site with reflectors on three of its four sides. This site clearly does not agree with the measured results with the average rms delay spread being 213 ns compared with 132 ns for the measured results. Sites 1.2 and 1.3 both use the same surround as in site 1.1 but obstacles

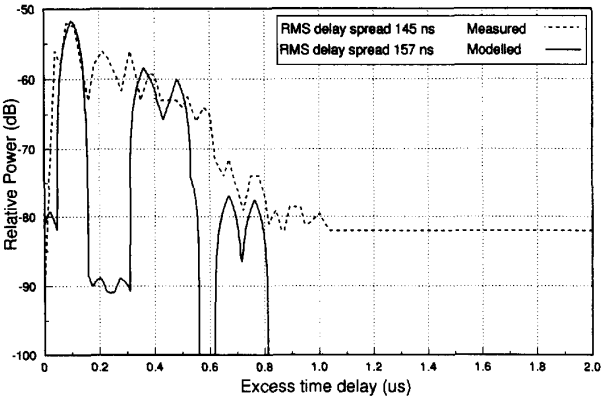

Fig. 24. Modeled and measured power delay profiles for an obstructed location (OBS) in site 3.

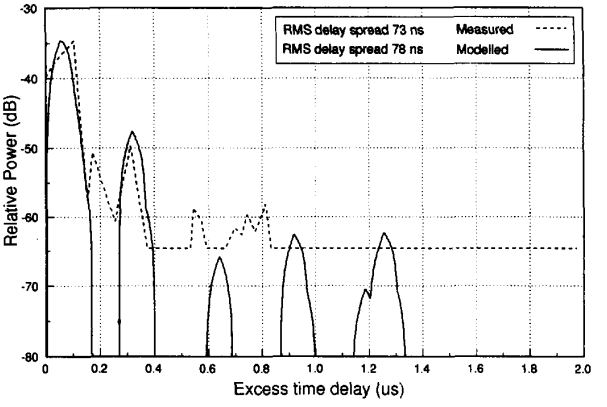

Fig. 25. Modeled and measured power delay profiles for a line of sight (LOS) location in site 3.

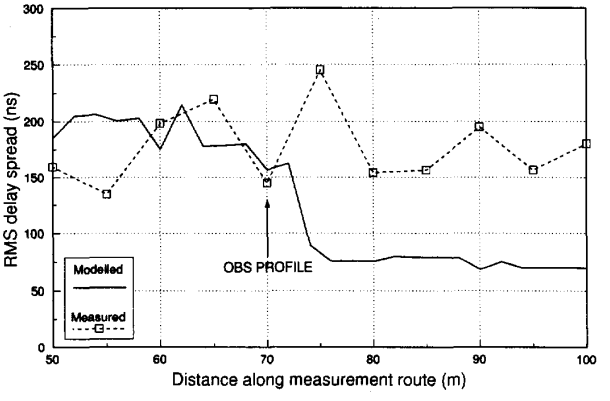

Fig. 26. Modeled and measured variation in rms delay spread with distance for site 3 along path A.

have been added within the medium. These two curves both give a reasonable fit; site 1.2 fits the curve well, except the model fails to find the very high values. Site 1.3 does not gives as close a fit for the earlier values but it does provide a more realistic maximum figure. The inability of the model

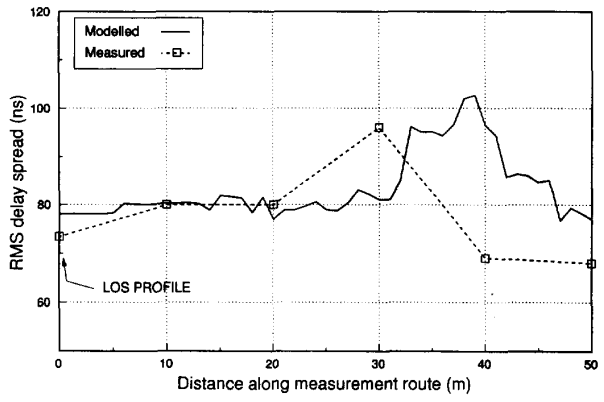

Fig. 27. Modeled and measured variation in rms delay spread with distance for site 3 along path B.

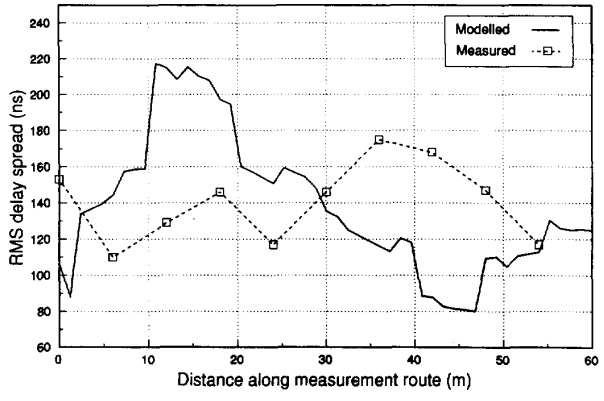

Fig. 28. Modeled and measured variation in rms delay spread with distance for site 3 along path C.

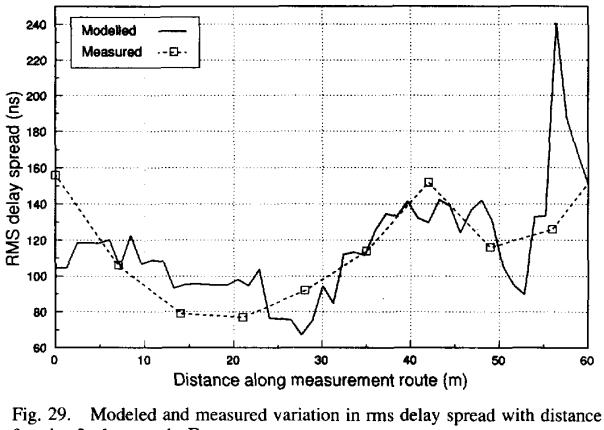

Fig. 29. Modeled and measured variation in rms delay spread with distance for site 3 along path D.

to predict the largest measured rms delay spread values is a weakness and probably arises because the model encloses the environment between bounding walls and hence may miss some distant reflected paths. As previously mentioned, the decision to use the bounding walls was made because it was felt that for the antenna heights considered here (Tx = 3.5

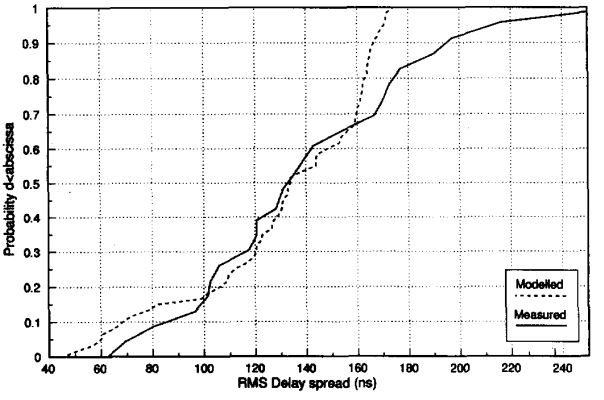

Fig. 30. Modeled and measured rms delay spread values for site 1.

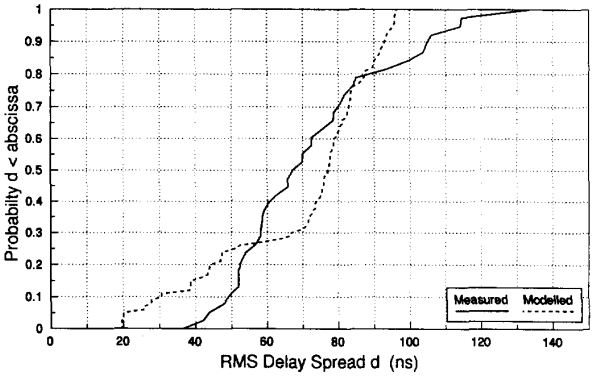

Fig. 31. Modeled and measured rms delay spread values for site 2.

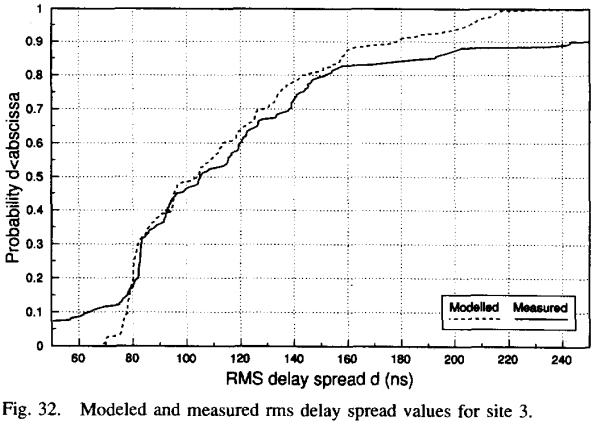

Fig. 32. Modeled and measured rms delay spread values for site 3.

m and Rx 1.5 m), it was more likely for a dissipating ray to encounter an interfering obstacle, such as a car, person, or tree, than to radiate into free space. For the results presented in this paper, it was decided to use site 1.3 because this gave the closest fit to the average rms delay spread.

A. Measurements and Model Validation

Measured and modeled power delay profiles were taken in all three sites and compared directly. Figs. 17–21 show power

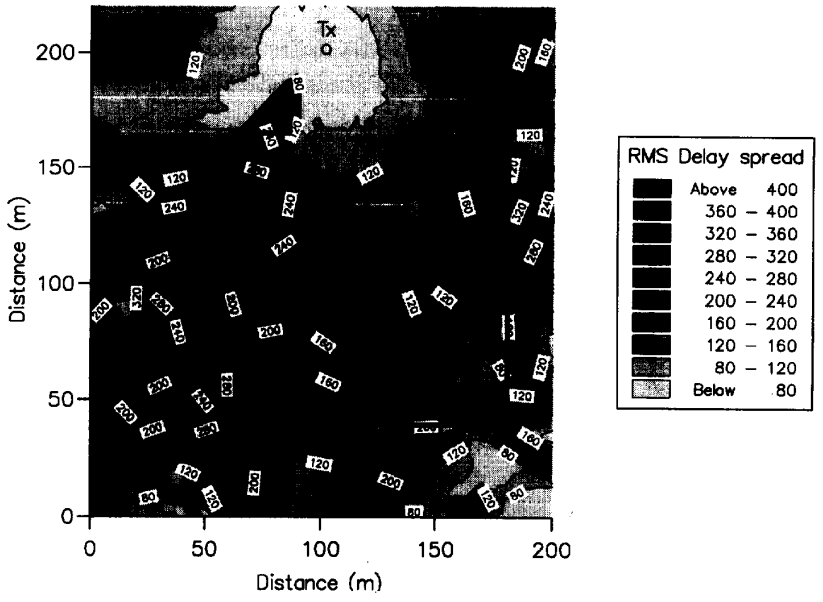

Fig. 33. Modeled variation in rms delay spread (ns) around site 1 (transmitter location).

delay profiles, for site 1 at locations A–E (see Fig. 12), and a summary of these results is given in Fig. 22. Each of these graphs shows three curves, two of which represent measured results and one modeled. The purpose of the two measured curves was to investigate the reproducibility of the power delay profile measurements. These results show similarities between the two sets of measurements (both taken on warm sunny days), although they do indicate that the rms delay spread figure is capable of varying quite significantly between readings and hence, there is a limit to the accuracy with which it can be quoted. It appears that in most cases the prediction algorithm is finding significant power at similar delays to the measured results (see Figs. 17–21). Perhaps the largest errors between the measured and modeled results are for delays directly following the line of sight (LOS) ray. This can be accounted for because the algorithm does not calculate scattered rays. Strong scattered paths arising from the LOS ray's interaction with obstacles arranged close to the receiver will therefore not be represented with the modeled results. In addition, there are discrepancies at some locations, in particular, positions B, D, and E, where a strong modeled path exists and the measured path is considerably weaker. This is probably due to the simplification of the site description within the model and the bounding walls used for the site.

The comparison of modeled and measured rms delay spread values (see Fig. 22) indicates that while the algorithm is finding values in a similar range to those measured, it is not always giving an accurate representation of specific rms delay spread values for given locations. In addition to this, the results indicate that the model is performing better for receiver locations which are close to the transmitter than for those where the separation is in excess of 100 m. This is thought to be due to the more complex propagation environment found with the more distant locations. For the locations very close

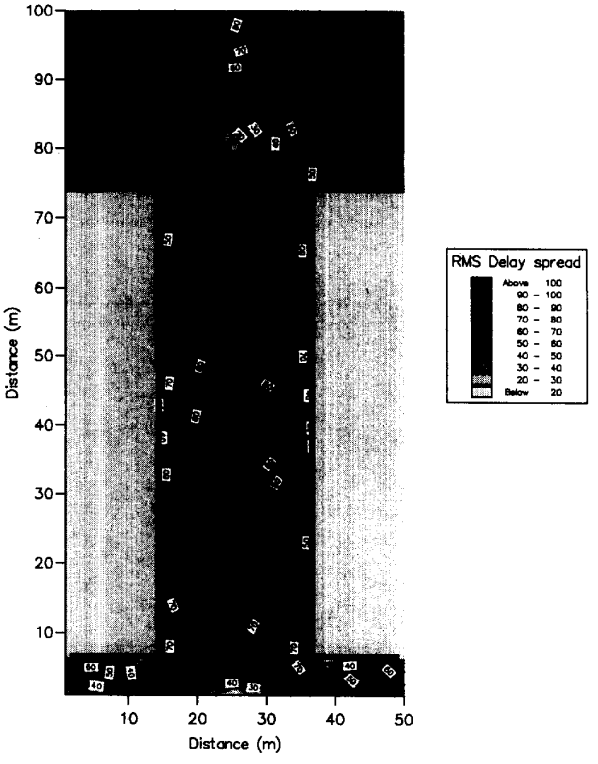

Fig. 34. Modeled variation in rms delay spread (ns) around site 2 (transmitter location indicated Tx).

to the transmitter, the power delay profiles in Figs. 17 and 18 show that there are very clearly two dominant paths. For the more distant locations, such as shown for position E in Fig. 21, the power delay profile is influenced by considerably

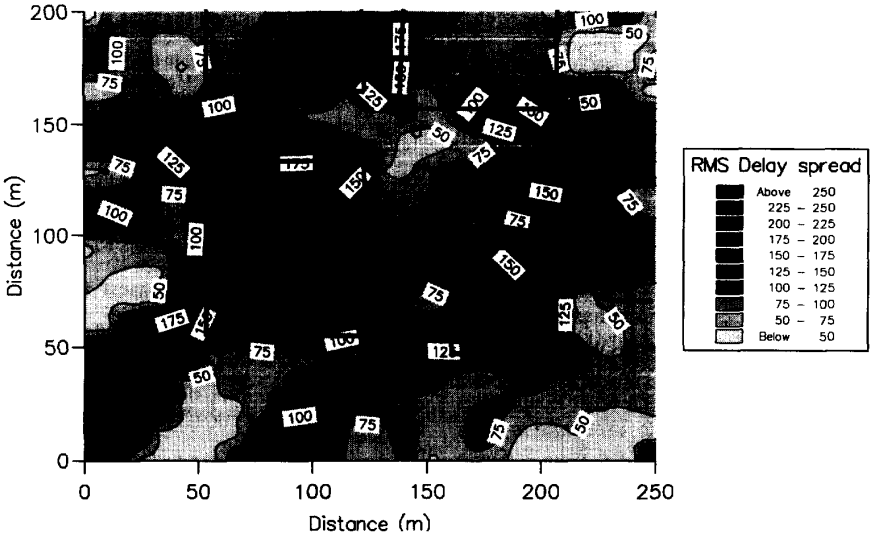

Fig. 35. Modeled variation in rms delay spread (ns) around site 3 (transmitter location indicated by Tx).

more significant paths. This more complex scenario has led both to bigger discrepancies between the two sets of measured results and the modeled values.

Fig. 23 shows delay spread versus distance for both the measured and modeled results taken for site 2. This figure indicates that, again, while the model evaluates typical values for the rms delay spread rather like the results for site 1, it is not able to predict localized variations. There would appear to be two principal reasons for this observation. First, the model does simplify the channel such that there is insufficient information to predict small scale details. Second, the measurement device works with a finite bandwidth so that, unlike the model, it experiences multipath effects for rays arriving with very short relative time delays. This results in fast fading effects for paths within *bins* in the power delay profile and hence a fluctuating rms delay spread value for small spatial movements. This effect would not be so apparent had averaging been performed with a slowly moving receiver. It is, however, apparent that both the measured and modeled results indicate that for this environment, the rms delay spread peaks at around 50 m from the transmitter and is lower both close to the transmitter and close to the building at the road end.

Finally, Figs. 24–29 all relate to measured and modeled results for site 3. Figs. 24 and 25 show measured and modeled power delay profiles, the former being for a sample obstructed (OBS) profile and the latter showing a line of sight (LOS) profile (see Fig. 14 for LOS and OBS locations). For the OBS profile, the model predicts a similar rms delay spread figure to the measured profile, but the profile does not contain as many paths as that found with the measurements. In addition, Figs. 26–29 (note these curves show the location of the LOS and OBS measured and modeled profiles) show modeled and measured rms delay spread values along the four measurement routes outlined in the description of site 3 (see Fig. 14). These figures show a reasonable agreement between measured and modeled results, with the exception of path *A* (shown in Fig. 26) where the measured results are greater than those calculated by the model. These inaccuracies have arisen because the receiver has moved into a heavily shadowed area and so that the model is failing to find enough rays to represent accurately the rms delay spread figure. In order to get over these errors, it is necessary to consider both the scattered rays and perhaps more orders of reflection. In addition, inaccuracies exist between the modeled and measured results which have arisen as a result of the simplifications of the cell environment, and this factor may be having some impact here.

V. Wideband Modeling Results

The cumulative distribution of the rms delay spread values is shown in Figs. 30–32. The modeled and measured results agree quite closely in each case. The smallest rms delay spread values are found in site 2 which, not surprisingly, is the smallest cell. Here, there is an rms delay spread range between 40 ns and 130 ns, with a median value of about 70 ns. Cell sites 1 and 3 both have similar dispersion characteristics ranging from 60 ns to 250 ns. Cell 1 has a slightly higher median value at 130 ns, compared to 120 ns for cell 3. Again, an agreement can be found between the modeled and measured results.

While it is apparent that modeled and measured rms delay spread values have similar distributions, the modeled results all indicate a lower maximum rms delay spread than that of the measured data. This is primarily because the model confines the environment to a finite size and restricts itself to calculating a maximum of seven orders of reflection. As a result, the model may fail to evaluate occasional paths from distance reflectors, and it is these paths which will typically contribute to give unusually large rms delay spread values.

Figs. 33, 34 and 35 all show the variation of rms delay spread contours for each of the three sites. These plots were generated in order to provide insight into the factors affecting the rms delay spread so that design choices and optimizations could be made. It is difficult to form many concrete design rules from these plots, but it is evident that there is a correlation between rms delay spread and shadowing, with increased rms delay spread figures in shadowed locations.

VI. Conclusions

A reflection and diffraction based algorithm has been shown to be a useful tool for the prediction of rms delay spread values for a range of different outdoor cordless environments. The algorithm uses an environmental description of particular sites for different applications typical of a cordless scenario in order to evaluate deterministically rms delay spread values. These are then presented, along with measured results, to demonstrate the model's ability to predict typical values.

Acknowledgment

The authors would like to thank SERC and BT laboratories for the award of an SERC CASE research studentship. In addition, they are grateful to BT for the provision of their channel sounding and laboratory facilities and, in particular, they are grateful for the assistance of P. R. Tattersall, Head of Mobile Propagation Group at BT laboratories, and Dr. M. P. Swinburne, formerly of BT laboratories. Finally, the authors are indebted to their colleagues at the Centre for Communications Research, University of Bristol, for the valuable advice and comments, and for provision of computing facilities.

References

[1] A. R. Nix and J. P. McGeehan, "Modeling and simulation of frequency selective fading using switched antenna diversity," *Electron. Lett.*, vol. 26, pp. 1868–1869, Oct. 1990.

[2] R. L. Davies, A. Simpson, and J. P. McGeehan, "Propagation measurements at 1.7 GHz for microcellular urban communications," *Electron. Lett.*, vol. 26, pp. 1053–1054, July 1990.

[3] D. C. Cox, "Delay Doppler characteristics of multipath propagation at 910 MHz in a suburban mobile radio environment," *IEEE Trans. Antenn. Propagat.*, vol. AP-20, pp. 625–635, Sept. 1972.

[4] D. M. J. Devasirvatham, "Time delay spread and signal level measurements of 850 MHz radio waves in building environments," *IEEE Trans. Antenn. Propagat.*, vol. AP-34, pp. 1300–1305, Nov. 1986.

[5] M. Bensebti, R. Davies, M. A. Beach, J. P. McGeehan, and D. C. Rickard, "Short range propagation measurements and modeling at 60 GHz for LAN's," presented at the *MIOP Int. Conf.*, Stuttgart, Germany, Sept. 1990.

[6] G. L. Turin, F. D. Clapp, T. L. Johnston, S. B. Fine, and D. Lavry, "A statistical model for urban multipath propagation," *IEEE Trans. Veh. Technol.*, vol. VT-21, pp. 1–9, Feb. 1972.

[7] H. Suzuki, "A statistical model for urban radio propagation," *IEEE Trans. Commun.*, vol. COM-25, pp. 673–680, July 1977.

[8] H. Hashemi, "Simulation of the urban radio propagation channel," *IEEE Trans. Veh. Technol.*, vol. VT-28, pp. 213–225, Aug. 1979.

[9] R. Ganesch and K. Pahlavan, "Statistical modeling and computer simulation of indoor radio channel," *IEE Proc. I.*, vol. 138, pp. 153–161, June 1991.

[10] T. S. Rappaport, S. Y. Seidel, and K. Takamizawa, "Statistical channel impulse response models for factory and open plan building radio communication system design," *IEEE Trans. Commun.*, vol. 39, pp. 794–807, May 1991.

[11] J. Zander, "A stochastical model of the urban UHF radio channel," *IEEE Trans. Veh. Technol.*, vol. VT-30, pp. 145–155, Nov. 1981.

[12] A. S. Bajwa, "A simple stochastic approach to wideband modelling of multipath propagation in mobile radio environments," presented at the *IERE Int. Conf. on Land Mobile Radio*, Cambridge, Aug. 1983.

[13] K. J. Gladstone and J. P. McGeehan, "Computer simulation of multipath fading in the land mobile radio environment," *IEE Proc.*, pt. G, pp. 323–330, Dec. 1980.

[14] ——, "A computer simulation of the effect of fading on a quasi-synchronous sideband diversity AM mobile radio scheme," *IEEE J. Select. Areas Commun.*, vol. SAC-2, pp. 191–203, Jan. 1984.

[15] M. C. Lawton and J. P. McGeehan, "The application of GTD and ray launching techniques to channel modeling for cordless radio systems," in *Proc. 1992 IEEE Veh. Technol. Conf.*, Denver, CO, May 1992, pp. 125–130.

[16] K. R. Schauback, N. J. Davis, and T. S. Rappaport, "A ray tracing method for predicting path loss and delay in microcellular environments," in *Proc. 1992 IEEE Veh. Technol. Conf.*, Denver, CO, May 1992, pp. 932–935.

[17] P. F. M. Smulders and M. A. A. Melters, "On the multipath behavior of mm-wave indoor radio channels," presented at the *European Cooperation in the field of Scientific and Technical Research*, COST 231, Paris, France, Oct. 1990.

[18] C. A. Balanis, *Advanced Engineering Electromagnetics*. New York: Wiley, 1989.

[19] M. Lebherz, W. Wiesbeck, and W. Krank, "A versatile wave propagation model for the UHF/VHF range considering 3-D terrain," presented at the *European Cooperation in the field of Scientific and Technical Research*, COST 231-TD(91), Firenze, Italy, Jan. 1991.

[20] V. Erceg, S. Ghassenzadeh, M. Taylor, D. Li, and D. Schilling, "Urban suburban out-of-sight propagation modeling," *IEEE Commun. Mag.*, vol. 30, pp. 56–61, June 1992.

[21] M. C. Lawton, R. L. Davies, and J. P. McGeehan, "An analytical model for indoor multipath propagation in the picocellular environment," in *Proc. 6th Int. Conf. Mobile Radio and Personal Commun.*, Warwick, UK, Dec. 1991, pp. 1–8.

[22] J. C. Schelling, C. R. Burrows, and E. B. Ferrell, "Ultra-short wave propagation," *Bell Syst. Tech. J.*, vol. 12, pp. 125–161, Apr. 1933.

[23] J. B. Keller, "Geometric theory of diffraction," *J. Opt. Soc. Amer.*, vol. 52, pp. 116–130, Feb. 1962.

[24] R. G. Kouyouijian and P. H. Pathak, "A uniform geometric theory of diffraction for an edge in a perfectly conducting surface," *Proc. IEEE*, vol. 62, pp. 1448–1461, Nov. 1974.

[25] R. J. Leubbers, "Finite conductivity uniform GTD versus knife edge diffraction in prediction of propagation path loss," *IEEE Trans. Antenn. Propagat.*, vol. AP-32, pp. 70–76, Jan. 1984.

[26] J. D. Parsons, D. A. Demery, and A. M. D. Turkmani, "Sounding techniques for wide-band mobile radio channels: A review," *IEE Proc. I*, vol. 138, pp. 437–446, Oct. 1991.

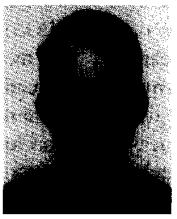

Michael C. Lawton was born in Whitehaven, UK, on April 30, 1967. He received the B.Eng. degree in electrical and electronic engineering from the University of Bristol, UK, after in 1989. He recenly received the Ph.D. degree at the Center for Communications Research, University of Bristol, UK, after studying deterministic approaches to propagation prediction for small cell systems. His Ph.D. program was sponsored by British Telecom Research Laboratories, UK, through a CASE award.

In 1992, he joined the Mobile Communications Department of Hewlett-Packard Laboratories, Bristol, UK. His current research interests lie in RF receiver design and radio access techniques for both wide and local area applications.

J. P. McGeehan received the B.Eng. degree and the Ph.D. degree in electrical and electronic engineering from the University of Liverpool, UK, in 1967 and 1971, respectively.

In 1970, he was appointed Senior Scientist at the Allan Clark Research Center, Plessey Company Limited, where he was responsible for the research and development of two- and three-terminal Gunn effect devices and their application to high-speed logic, telecommunications and radar systems. In 1972, he became a Member of the Academic Staff of the School of Electrical Engineering of the University of Bath and initiated research in the area of SSB (subsequently linear modulation) for mobile radio. In 1984, he was appointed to the Chair of Communications Engineering at the University of Bristol. He is presently Head of the Department of Electrical and Electronic Engineering and Director of the University Research Center in Communications Engineering.

Dr. McGeehan is the recipient of the IEE Proceedings Mountbatten Premium and the IEEE Transactions Neal Shephard Award, and he has received a number of other awards in recognition of his research contribution to radio communications from other organizations such as the Motorola Research Foundation (USA) and Schlumberger Industries (France). He is a Fellow of the IEE, a Fellow of the Royal Society of Arts and Commerce, and serves on numerous national and international committees concerned with mobile communications. In July 1994, he was elected Fellow of the Royal Academy of Engineering.